AIMS Mathematics, 10(11): 27381–27411.
DOI: 10.3934/math.20251204
Received: 17 September 2025
Revised: 01 November 2025
Accepted: 10 November 2025
Published: 25 November 2025

https://www.aimspress.com/journal/Math

Research article

Adaptive neuro-fuzzy inference system prediction of thermal transport in Casson ternary hybrid nanofluid thin film flow for biomedical applications

Maddina Dinesh Kumar[1,†], S. Mamatha Upadhya[2], Nehad Ali Shah[1,†], C. S. K. Raju[4] and Se-Jin Yook[1,*]

[1] School of Mechanical Engineering, Hanyang University, 222 Wangsimni-ro, Seongdong-gu, Seoul 04763, Republic of Korea
[2] Faculty of Mathematics, Institute of Management, Kristu Jayanti University, Kothanur, Bengaluru, Karnataka 560077, India
[3] Department of Mechanical Engineering, Sejong University, Seoul 05006, South Korea
[4] Department of Mathematics, School of Computer Science and Artificial Intelligence, SR University, Warangal-506371, Telangana, India

[†]These authors contributed equally to this work and are co-first authors.

* **Correspondence:** Email: ysjnuri@hanyang.ac.kr.

Abstract: In this work, the adaptive neuro-fuzzy inference system (ANFIS) and particle swarm optimization (PSO) were used to anticipate the behavior of heat transfer in ternary hybrid nanofluid flow through thin films. For intricate heat transfer processes in nanofluid applications, the combined ANFIS-PSO model improved forecast accuracy. The simulated PDEs were converted into ODEs by varying similarity factors. A ternary hybrid nanofluid across the surface, radiation, heat source/sink, and non-uniform magnetic field were used to theoretically examine the unique properties of unstable thin film flow; nanoparticles, namely $MWCNT$, $SWCNT$, and TiO_2, were used in both the Casson and non-Casson scenarios, using the base fluid, blood. The ANFIS-PSO models were trained using the numerical results from MATLAB's built-in BVP4C function to control the complexity and predict the results. Plotting and analysis were done to see how various flow parameters affect temperature, velocity, and heat transfer. A ternary hybrid nanofluid without a Casson scenario had a higher Nusselt number, per the study's conclusions, than a Casson ternary nanofluid with blood as the base fluid with nanoparticles $SWCNT + TiO_2 + MWCNT$. It was discovered that the truth values are accurately

predicted by ANFIS-PSO models, and in most of the runs in Table 3, in Case-2, the rate of heat transmission is 1% higher than in Case-1.

Keywords: heat source/sink; radiation; magnetohydrodynamics (MHD); thin film; optimization of particle swarms with an adaptive neuro-fuzzy inference system
Mathematics Subject Classification: 76A02, 76A05, 76A20, 76W05

1. Introduction

In numerous engineering and industrial procedures, boundary layer flow and heat transmission phenomena in thin films hold significant applications, such as in wire coating, aerodynamic extrusion of the plastic sheet, polymer and metal extrusion, coating of fiber, and processing of meals. Wang [1] initiated studies on the hydrodynamics of flow in thin liquid sheets with unstable stretching surfaces that are unstable. His innovative research was further developed by Andersson et al. [2] and Abel et al. [3]. Kumar et al. [4] investigated how MHD nanofluid flow across a thin film is affected by irregular radiation and heat sources. They found that, compared to ferrofluid, the hybrid ferrofluid had a higher rate of heat transmission. Prasad et al. [5] reported the influence of nonlinear convection, thermocapillary, varying viscosity, and thermal conductivity in heat transfer through an unstable thin-film flow. Gomathy and Kumar et al. [6] observed porosity and magnetic field-enhanced skin friction in unsteady nanofluid flow in a thin film. Bhandari et al. [7] described the influence of variable thickness in bioconvective nanofluids. Wang et al. [8] investigated velocity slip in the thin film and mass and heat transport in a silver water nanofluid. They observed that the concentration and thermophoresis-enhanced nanofluid temperature. Qayyum et al. [9] applied fuzzy calculus to examine the nanofluid flow in a thin film. Pal and Chatterjee [10] addressed heat transport in Casson nanofluid with chemical reactions, fluctuating heat conductivity, and the dissipation of a viscous fluid through a thin film with unstable stretching surfaces.

Non-Newtonian fluid is significantly more complicated and non-linear than Newtonian fluid. Thus, all properties of these fluids cannot be expressed with a single constitutive equation. Hence, many researchers have developed various models to symbolize the fluid that is not Newtonian. The Casson fluid model is one case of such a model examined in relation to biomedical applications by Bathmanaban et al. [11]. Dash et al. [12] showed that because red blood cells include protein, fibrinogen, and globulin, human blood is likewise a Casson fluid and aqueous-based plasma. The Casson fluid is by far the most well-known non-Newtonian fluid, which has wide applications in bioengineering, drilling, metallurgy, food processing, etc. Alghamdi et al. [13] examined employing cobalt doping to modify the microstructure and thermoelectric response of the β-$FeSi_2$ thin film, and Duraihem et al. [14] explained the Casson fluid's flow properties along curved stretching surfaces. Fahmy et al. [15] investigated a computerized DRBEM model for generalized magneto-thermo viscoelastic stress waves in anisotropic thin film/substrate systems that are functionally graded. Thenmozhi et al. [16] deliberated Lie similarity analysis, overstretching of a porous sheet in MHD Casson fluid, combined with a changing viscosity and heat source.

Due to rapid growth in industry and a flourishing population, global energy consumption is experiencing a gigantic rise. Urbanization increases as industries expand, leading to a surge in infrastructure and intensive technologies. This creates massive pressure on both non-renewable and

renewable energy resources. To safeguard long-term sustainability, deploying adequate energy via measures such as implementing renewable energy and advanced energy management systems is necessary. Using energy effectively reduces greenhouse emissions, resource depletion, and cost and endorses future energy security. Researchers have proved that the advancement and application of nanoparticles in conventional fluids would help improve thermal performance and save energy. The invention of nanofluid could have occurred during the mid-1990s when Choi [17] and his teammates at Argonne National Laboratory (United States) introduced this novel concept. The fluid's heat capacity, heat transfer, and thermal conductivity are greatly increased by the immersion of nanoparticles, which are usually oxides, metals, and carbon-based compounds. High-performance SnS thin films that are bi-doped: An approach to increasing thermoelectric power for tiny gadgets was looked into by Hakami et al. [18]. Upadhya et al. [19] investigated a spinning disk utilising a ternary hybrid nanofluid and Joule heating. Krishna et al. [20] predicted how ternary hybrid nanofluid affects heat and mass transmission. Kumar and Hassan [21] examined how well a ternary hybrid nanofluid performed in a flat tube. Mishra and Pathak [22] compared hybrid and ternary hybrid nanofluids across inclined cylinders. Mohana and Kumar [23] analytically investigated ternary hybrid nanofluid properties and nature in parallel surfaces. Mohanty et al. [24] determined that the ternary hybrid nanofluid along a stretching cylinder had a higher entropy. The rate at which the body emits /absorbs thermal radiation depends on its surface. In a vacuum, radiation is the most effective heat transport mechanism. Any matter having a temperature above absolute zero radiates energy, acknowledged as thermal radiation. The radiation effect finds abundant application in space technology, polymer processing, glass production, nuclear reactors, gas turbines, etc. Rana et al. [25] examined how to use the Taguchi method to optimize heat transfer through nonlinear thermal convection flow over a solid sphere with Stefan blowing and thermal slip. Rana et al. [26], examined the stability and multiplicity of solutions in non-Newtonian Carreau nanofluid transport phenomena using neural prediction and nonlinear Rosseland thermal approximations. Ramesh et al. [27] used a neural network algorithm to analyze the ternary hybrid nanofluid along the Riga surface. Rana et al. [28] investigated the energy system with conductive solid body and bottom circular heaters using a hybrid nanofluid of Ag MgO (50:50), and water was calculated using finite element and neural calculations.

Research questions of this study:

1) Can a ternary hybrid nanofluid enhance the heat transfer rate?
2) Integrating ANFIS with PSO will enhance the prediction accuracy?
3) How inclined magnetic field effect the flow profiles?
4) Can ANFIS-PSO accurately predict the numerical results?
5) Which case has a higher heat transfer rate, with Casson or without Casson?
6) How do non-uniform heat sources impact the flow regimes?

Novelty of this study:

Inspired by the above-mentioned studies, we compared a ternary hybrid nanofluid in this paper with blood as the base fluid, with $\left(SWCNT + TiO_2 + MWCNT\right)$ nanoparticles scenarios with Casson and without Casson flow through a thin film with the impacts of MHD, including radiation and an uneven heat source or sink. Numerical results are obtained from MATLAB software with the BVP4C solver, and the heat transfer rate truth values are predicted using ANFIS-PSO. The outcome of this investigation could enhance heat transference in technical and industrial applications.

2. Mathematical modeling

An extended sheet is believed to be traversed by a ternary hybrid nanofluid in the (x, y) depiction of the coordinate system in Figure 1. Here, the stretched sheet moved with velocity at the wall $u_w = bx/(1-\alpha t)$, $T_w = T_0 - \left(bx^2/2\nu_f\sqrt{(1-\alpha t)}\right)T_r$ is the wall's temperature near it, a magnetic field that changes with time $B = (1-\alpha t)^{-0.5} B_0$ is regarded as:

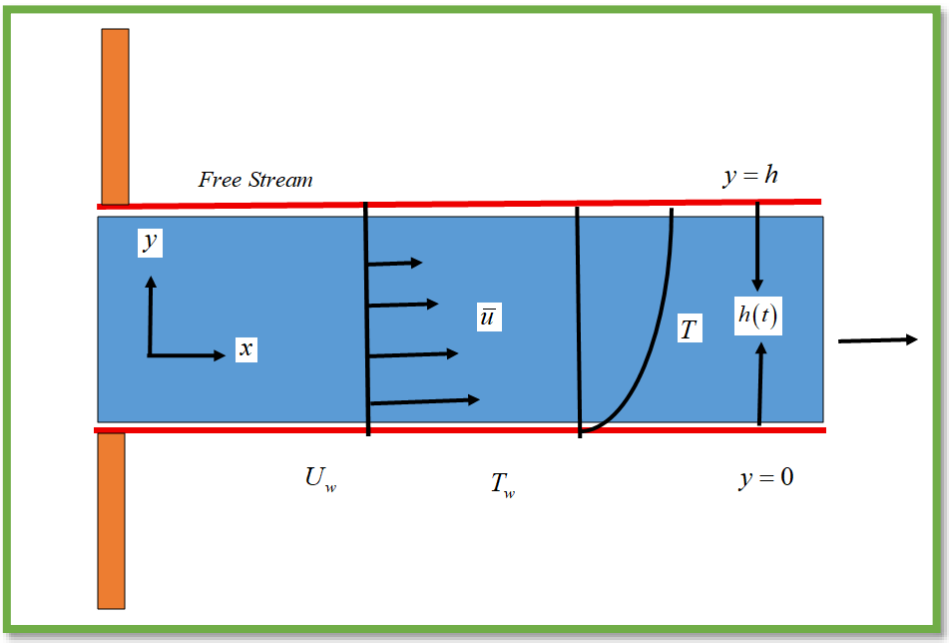

Figure 1. Flow geometry.

The flow equations are given under the aforementioned assumptions using the study of Kumar et al. [4], Gul et al. [29], and Ali et al. [30].

The equation for continuity

$$\frac{\partial \bar{v}}{\partial y} + \frac{\partial \bar{u}}{\partial x} = 0. \tag{1}$$

The momentum equation

$$\rho_{THNF}\left(\bar{v}\frac{\partial \bar{u}}{\partial y} + \frac{\partial \bar{u}}{\partial t} + \bar{u}\frac{\partial \bar{u}}{\partial x}\right) = \mu_{THNF}\frac{\partial^2 \bar{u}}{\partial y^2}\left(1 + \frac{1}{\beta_1}\right) - \sigma_{THNF}B_0^2\left(\mathrm{Cos}^2\,\omega\right)\bar{u}. \tag{2}$$

Equation of energy

$$\left(\rho c_p\right)_{THNF}\left(\bar{u}\frac{\partial T}{\partial x} + \bar{v}\frac{\partial T}{\partial y} + \frac{\partial T}{\partial t}\right) = \frac{\partial^2 T}{\partial y^2}\left(k_{THNF} + \frac{16T_\infty^3\sigma^*}{3k^*}\right) + \mu_{THNF}\left(\frac{\partial \bar{u}}{\partial y}\right)^2 + q'''. \tag{3}$$

The requirements for the problem that was designed using the study by Kumar et al. [4]

$$\begin{aligned} &T = T_w, \bar{v} = 0, \bar{u} = u_w \qquad \text{at} \quad y = 0 \\ &\frac{\partial \bar{u}}{\partial y} = \frac{\partial T}{\partial y} = 0 \quad \text{at} \quad v = \frac{\partial h}{\partial t}, y = h \text{ at } y = h(t), \end{aligned} \tag{4}$$

where σ^* represents the Boltzmann-Stein constant, k^* is the average absorption constant, and $h(t)$ is the film's thickness.

The irregular heat source or sink q''' is given by

$$q''' = \frac{\bar{u}_w k_f (T_w - T_0)}{x \nu_f} \left(f' * A + \frac{(T - T_0)}{(T_w - T_0)} * B \right). \tag{5}$$

Here, B and A Heat sources and sinks throughout the body are represented by increasing and decreasing numbers, respectively.

The ternary hybrid nanofluid's viscosity is

$$\mu_{THNF} = \frac{\mu_f}{\left(-\varphi_{TiO_2} + 1\right)^{2.5} \left(1 - \varphi_{SWCNT}\right)^{2.5} \left(1 - \varphi_{MWCNT}\right)^{2.5}}. \tag{6}$$

Density model of ternary hybrid nanofluid

$$\begin{aligned} \frac{\rho_{THNF}}{\rho_f} &= \left(1 - \varphi_{SWCNT}\right) \left\{ \left(1 - \varphi_{TiO_2}\right) \left[\left(1 - \varphi_{MWCNT}\right) + \frac{\varphi_{MWCNT} \rho_{MWCNT}}{\rho_f} \right] + \frac{\varphi_{TiO_2} \rho_{TiO_2}}{\rho_f} \right\} \\ &+ \frac{\varphi_{SWCNT} \rho_{SWCNT}}{\rho_f}. \end{aligned} \tag{7}$$

The following is the specific heat model for the ternary hybrid nanofluid

$$\frac{\left(\rho c_p\right)_{THNF}}{\left(\rho c_p\right)_f} = \varphi_{SWCNT} \frac{\left(\rho c_p\right)_{SWCNT}}{\left(\rho c_p\right)_f} + \left(1 - \varphi_{SWCNT}\right) \left[\begin{array}{l} \left\{ \dfrac{\left(\rho c_p\right)_{MWCNT}}{\left(\rho c_p\right)_f} \varphi_{MWCNT} + \left(1 - \varphi_{MWCNT}\right) \right\} \\ \left(1 - \varphi_{SWCNT}\right) + \varphi_{TiO_2} \dfrac{\left(\rho c_p\right)_{TiO_2}}{\left(\rho c_p\right)_f} \end{array} \right]. \tag{8}$$

The thermal conduction model of ternary hybrid nanofluids is

$$\left.\begin{aligned}
\frac{k_{THNF}}{k_{hnf}} &= \frac{\left(k_{MWCNT}+2k_{hnf}-2\varphi_{MWCNT}\left(k_{hnf}-k_{MWCNT}\right)\right)}{\left(k_{MWCNT}+2k_{hnf}+\varphi_{MWCNT}\left(k_{hnf}-k_{MWCNT}\right)\right)}\\
\frac{k_{hnf}}{k_{nf}} &= \frac{\left(2k_{nf}+k_{TiO_2}-\left(k_{nf}-k_{TiO_2}\right)2\varphi_{TiO_2}\right)}{\left(2k_{nf}+k_{TiO_2}+\left(k_{nf}-k_{TiO_2}\right)\varphi_{TiO_2}\right)}\\
\frac{k_{nf}}{k_f} &= \frac{\left(2k_f+k_{SWCNT}-\left(\sigma_f-k_{SWCNT}\right)2\varphi_{SWCNT}\right)}{\left(2k_f+k_{SWCNT}+\left(k_f-k_{SWCNT}\right)\varphi_{SWCNT}\right)}
\end{aligned}\right\}. \tag{9}$$

The model for the electric conductivity of ternary hybrid nanofluids is

$$\left.\begin{aligned}
\frac{\sigma_{hnf}}{k_{nf}} &= \frac{\left(\sigma_{TiO_2}+2\sigma_{nf}-2\varphi_{TiO_2}\left(\sigma_{nf}-\sigma_{TiO_2}\right)\right)}{\left(\sigma_{TiO_2}+2\sigma_{nf}+\varphi_{TiO_2}\left(\sigma_{nf}-\sigma_{TiO_2}\right)\right)}\\
\frac{\sigma_{Thnf}}{\sigma_{hnf}} &= \frac{\left(2\sigma_{hnf}+\sigma_{MWCNT}-2\left(\sigma_{hnf}-\sigma_{MWCNT}\right)\varphi_{MWCNT}\right)}{\left(2\sigma_{hnf}+\sigma_{MWCNT}+\varphi_{MWCNT}\left(\sigma_{hnf}-\sigma_{MWCNT}\right)\right)}\\
\frac{\sigma_{nf}}{\sigma_f} &= \frac{\left(\sigma_{SWCNT}+2\sigma_f-2\varphi_{SWCNT}\left(\sigma_f-\sigma_{SWCNT}\right)\right)}{\left(\sigma_{SWCNT}+2\sigma_f+\varphi_{SWCNT}\left(\sigma_f-\sigma_{SWCNT}\right)\right)}
\end{aligned}\right\}. \tag{10}$$

Here, φ represents the hybrid nanoparticles' volume proportion, and $\varphi_1,\varphi_2,\varphi_3$ show the percentage of volume for each unique nanoparticle.

Here, the suffixes $THNF, f, s$ describe the solid particles, a Ternary hybrid nanofluid with a base fluid.

In light of the situation, the analogies are used as:

$$\left.\begin{aligned}
&\xi=\frac{1}{\beta}\left(\frac{b}{\nu_f\left(1-\alpha t\right)}\right)^{0.5} y,\psi=\beta\left(\frac{\nu_f b}{\left(1-\alpha t\right)}\right)^{0.5} xf\left(\xi\right),\theta=\frac{\left(T-T_0\right)}{\left(T_w-T_0\right)},\\
&\bar{u}=\frac{\partial\psi}{\partial y},\bar{v}=-\frac{\partial\psi}{\partial x},T_w=T_0-T_r\left(\frac{bx^2}{2\nu_f}\right)\left(1-\alpha t\right)^{-1.5}\theta\left(\xi\right)
\end{aligned}\right\}. \tag{11}$$

Equations (2) and (3) are transformed using Eqs (5) and (11) as follows:

$$\left(1+\frac{1}{\beta_1}\right)B_1 f'''+B_2\lambda\left(f''-\left(f'\right)^2-Sf'-S\frac{\xi}{2}f''\right)-B_5\left(\mathrm{Cos}^2\,\omega\right)Mf'=0. \tag{12}$$

$$\left(B_3+\frac{4}{3}R\right)\theta''+\frac{B_1}{B_4}\Pr Ec\left(\frac{\partial f}{\partial \xi}\right)^2-\Pr B_4\lambda\left(\frac{S}{2}\left(\xi\theta'+3\theta\right)-f\theta'+2\frac{\partial f}{\partial \xi}\right)+B\theta+\frac{\partial f}{\partial \xi}A=0\,. \tag{13}$$

The boundary conditions of Eq (4) are transformed as follows using Eq (11):

$$\theta(\xi)=1, f(\xi)=0, f'(\xi)=1 \qquad at\ \ \xi=0$$
$$f(\xi)=S/2, f''(\xi)=0, \theta'(\xi)=0 \qquad at\ \ \xi=1$$

In Eqs (12) and (13), unsteady parameter (S), Radiation parameter (R), Prandtl number $(\Pr)$, Film thickness parameter (λ), Magnetic field parameter (M), and Eckert number Ec are defined as follows:

$$R=\frac{4\sigma^* T_0^3}{k^* k_f}, \Pr=\frac{\nu_f}{\alpha_f}, \lambda=\beta^2, M=\frac{\sigma_f B_0^2}{b\rho_f}, S=\frac{\alpha}{b}, Ec=\frac{u_w^2}{(Cp)_f\left(T_w-T_0\right)}.$$

The Nusselt number Nu_x is given by

$$\mathrm{Re}_x^{-0.5}\,Nu_x=\left(\frac{4R}{3}+\frac{k_{THNF}}{k_f}\right)\frac{-1}{\beta}\theta'(0).$$

Here, $\mathrm{Re}_x=\dfrac{\bar{u}_w x}{\nu_f}$ is Reynolds' number.

Equations (12) through (13) are taken into consideration below the assumptions.

$$B_1=\frac{\mu_{THNF}}{\mu_f}, B_2=\frac{\rho_{THNF}}{\rho_f}, B_3=\frac{k_{THNF}}{k_f}, B_4=\frac{(\rho Cp)_{THNF}}{(\rho Cp)_f}, B_5=\frac{\sigma_{THNF}}{\sigma_f}.$$

3. Numerical methodology

❖ **Describe the boundary value problem (BVP) as follows:** Specify the differential equations as a function that takes the independent variable x and solution vector y, and returns the derivatives $\dfrac{dy}{dx}$ Moreover, a distinct function that returns the residuals at boundaries defines the boundary conditions.

❖ **Make an initial guess:** Provide a rough estimate for the solution, including a rough estimate for particular mesh points. The bvpinit function in MATLAB can be used to set up this initial guess over a specified period of time.

❖ **Utilise BVP4C to resolve the BVP:** Utilize the differential equations function, boundary conditions function, and beginning guess to activate the BVP4C function. BVP4c iteratively solves the BVP using a collocation technique, adjusting the mesh as needed to attain precision.

❖ **Convergence criteria:** With tolerance error, the produced numerical ternary solution has a convergence criterion of 10^{-6}.

❖ **Extract and analyze results:** The output of bvp4c includes the solution structure with values at certain mesh points. Plotting and evaluating the answer using this output will enable further investigation or result visualization.

4. Results and discussion

4.1. Particle swarm optimization in conjunction with an adaptive neuro fuzzy inference system

The hybrid computational method, ANFIS-PSO, amalgamates neural networks, fuzzy logic, and optimization techniques, are used to improve prediction accuracy. It is helpful in control systems, predictive modeling, and pattern recognition by using the study of Divya et al. [31]. Figures 2–19 portray the output of simulated results of ANFIS-PSO, Quiver, Surface 3D plots for inputs, $M, S,$ and R regarding the blood-based ternary hybrid nanofluid in Case-1, with Casson, and the blood-based ternary hybrid nanofluid in Case-2, without Casson.

The investigation's flow geometry is depicted in Figure 1. The ANFIS-PSO neural network structure of Case-1 is shown in Figure 2, and it is observed that there is an excellent hybrid learning process that has a well-integrated network with well-knit layers. The obtained RMSE is 3.60764e-06, which proves the fine accuracy of the model prediction and good convergence level. Figure 3 shows the training error reduction of the ANFIS-PSO model in Case-1, where the error rate declines quickly in the early epochs and then remains constant after about 40 epochs. This is a sign of effective learning and excellent model stability with a small residual error. The ANFIS-PSO rule structure of Case-1 is in Figure 4, which depicts the interaction between the input membership functions and the output. As the figure confirms, the fuzzy rules have been optimized, resulting in the correct value of the output being 4.26, which shows that the model successfully utilizes the reasoning of the rules. Figure 5 illustrates how the *Nus-1* surface changes for parameters *S* and *R*. It is observed that the Nusselt number increases for both *S* and *R* levels, which suggests an increase in convective heat transfer. The enhanced *Nus-1* values in the red region testify to better thermal operation in these ranges of parameters. Figure 6 displays the *Nus-1* surface variance for the *R* and *M* parameters. The plot shows that there are some observable variations in the trend of the plot, suggesting that the rate of heat transmission is significantly influenced by both characteristics. An increase in the value of the Nusselt number indicated by the red states translates to a superior convective heat transfer activity. *Nus-1* surface variation with respect to parameters *M* and *S* is shown in Figure 7. It is observed that when the values of both parameters rise, the Nusselt number progressively rises, which implies that there is a better convective heat transfer. The red zone indicates the areas of high thermal performance in combined *M* and *S*. Figure 8 shows how the parameters *S* and *R* affect the quiver diagram of *Nus-1* in a particular direction, indicating that the variation in *S* and *R* has a great effect on the heat transfer rate and flow behavior of *Nus-1* through the strong gradient changes in the vector field. The *Nus-1* quiver plot is shown in Figure 9, and this gives the combined effect of the two parameters, *R* and *M*. The directional arrows show a significant change in gradient, which means that the change in *R* and *M* has a significant effect on the *Nus-1*-related flow dynamics and heat transfer intensity. Figure 10 shows the *Nus-1* quiver plot in which the interaction effects of parameters *M* and *S* are shown. The patterns of arrows with clear directional gradients demonstrate that changes in *M* and *S* have a substantial influence on the distribution and the intensity of the heat transfer rate Nus 1. Figure 11 depicts that the

ANFIS-PSO neural network structure of Case-2 exhibits good relationships between the input, rule, and output layers. The resulting RMSE of 3.675e-06 supports the fact that the hybrid model has a high level of prediction and strong learning performance. Figure 12 shows the convergence of the training error of the ANFIS-PSO model of Case-2. The error reduces significantly during the initial epochs, and it levels off after approximately 40 iterations. Such a steady decrease is a testimony to the great stability of the model with a small error and effective learning. Figure 13 displays the ANFIS-PSO rule representation of Case-2 with the interaction of the input membership functions and the output that is generated. The fuzzy rules are optimized to provide an accurate output of 4.32, which means that the model prediction performance of the model is reliable and that the fuzzy rules are adaptable. Figure 14 shows the surface variation of the *Nus-2* with respect to parameters *S* and *R* for Case-2. The plot indicates that an increase in the value of *S* and *R* results in an increase in the Nusselt number, which depicts a higher level of convective heat transfer. The yellow area is where the *Nus-2* is the greatest, indicating better thermal performance at this range.Figure 15 represents the surface variation of the *Nus-2* versus the parameters *R* and *M* of Case-2. The variations, imply that the two parameters have a strong impact on heat transfer. The yellow regions have higher values of the Nusselt number, which represents regions of higher performance of convective heat transfer. Figure 16 depicts the variation of the *Nus-2* as a surface variable of Case-2 with reference to parameters *M* and *S*. The Nusselt number becomes higher when the two parameter values are high, which means that it has better heat transfer performance. The yellow areas are the places of the highest *Nus-2* values, which have high convective effectiveness. Figure 17 quiver plot *Nus-2* illustrates how the *S* and *R* parameters have a directional influence. The arrow patterns exhibit high gradient variations, indicating that variations in *S* and *R* have a high influence on the amount and direction of heat transmission. Additionally, Figure 18 shows the *Nus-2* quiver diagram that shows the combined effect of the parameters *R* and *M*. Directional vectors that show observable variations in flow gradients prove the point that alterations in *R* and *M* play a significant role in determining the speed and distribution of heat transfer. The *Nus-2* quiver diagram of the interactive effects of parameters *M* and *S* is presented in Figure 19. The patterns of directional flow have changed significantly, which indicates that *M* and *S* are to determine the direction and magnitude of the heat transfer gradients in Case-2.

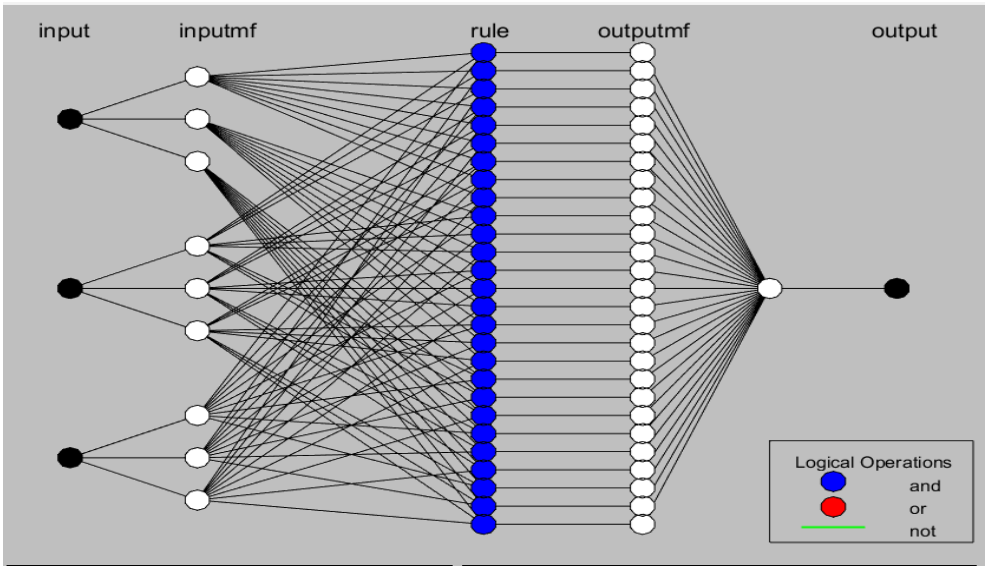

Figure 2. ANFIS-PSO neural network Case-1.

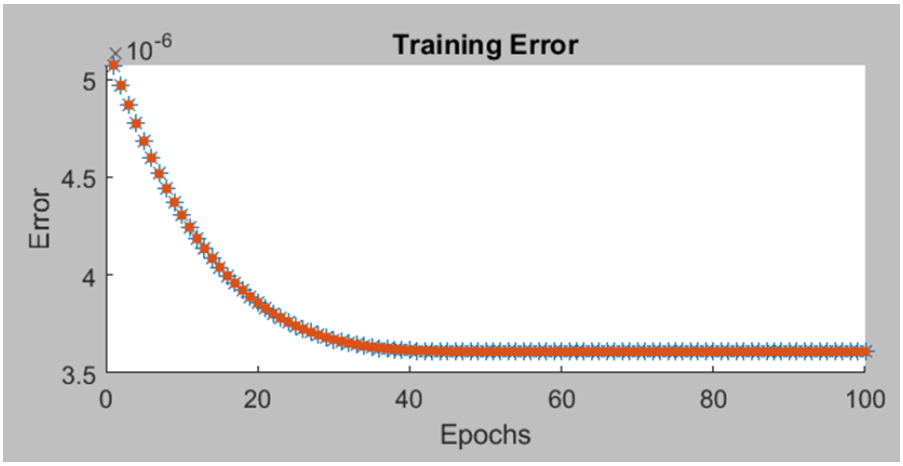

Figure 3. ANFIS-PSO Case-1 error, RMSE=3.60764e-06.

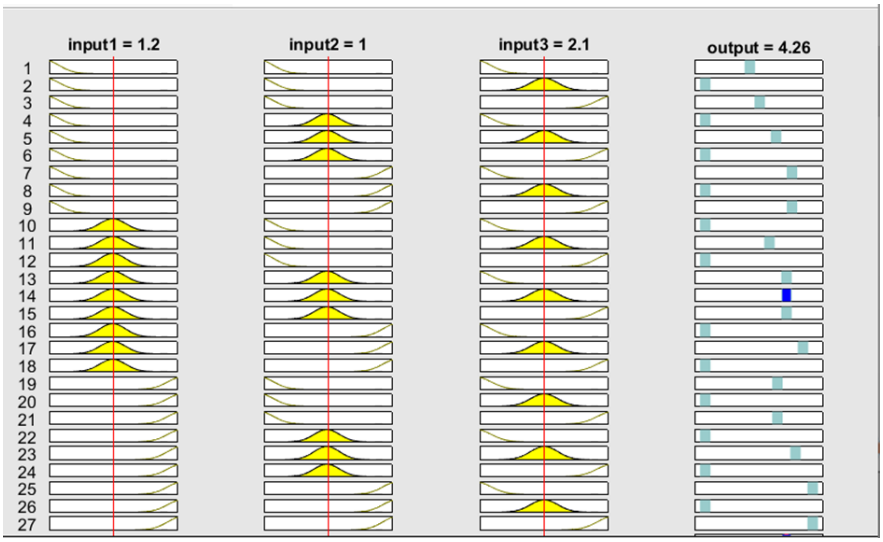

Figure 4. ANFIS-PSO Case-1 rules.

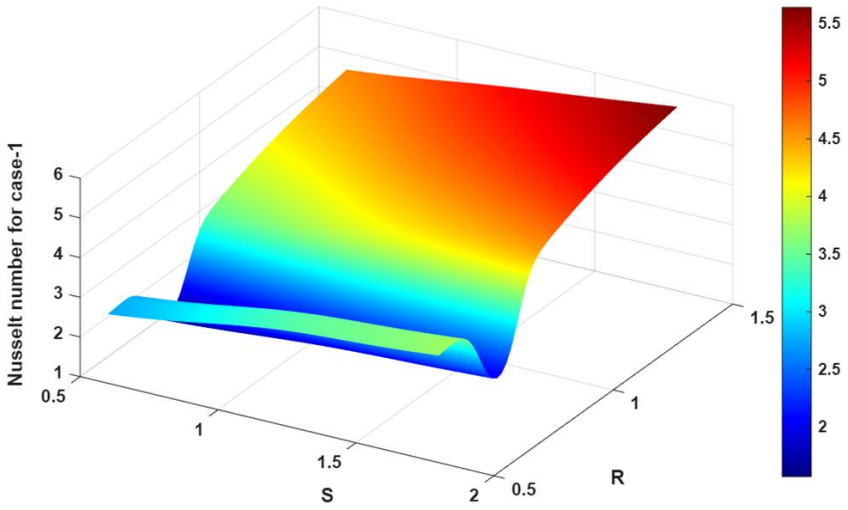

Figure 5. Surface plot of Nus-1 for S, R.

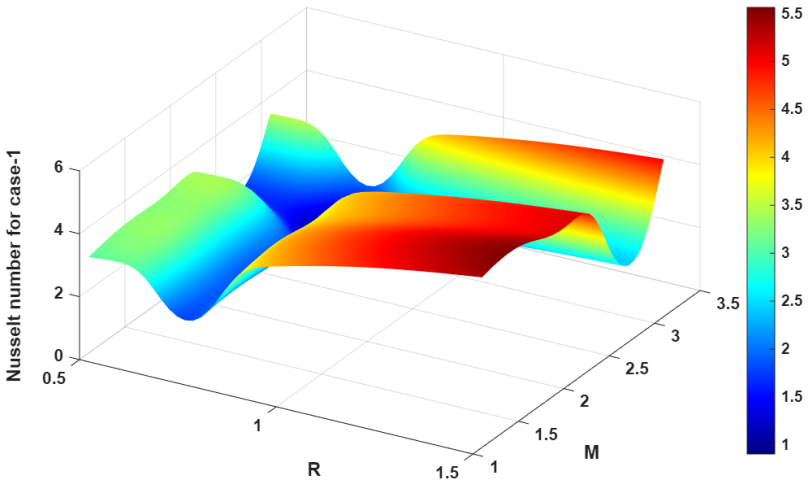

Figure 6. Surface plot of Nus-1 for R, M.

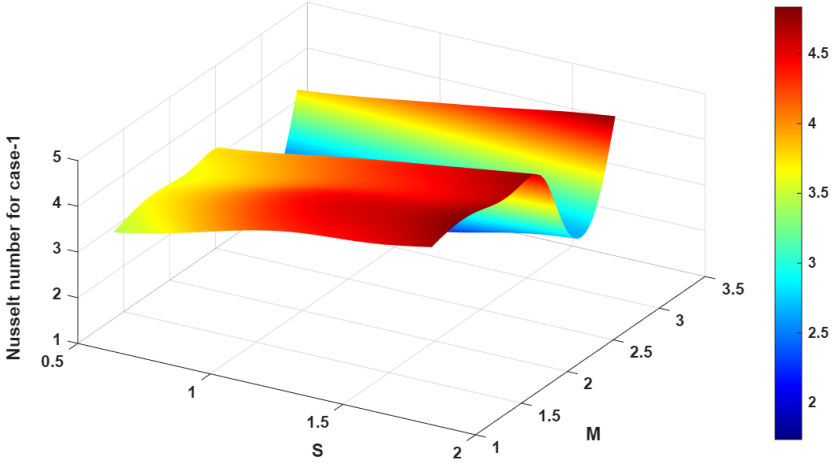

Figure 7. Surface plot of Nus-1 for M, S.

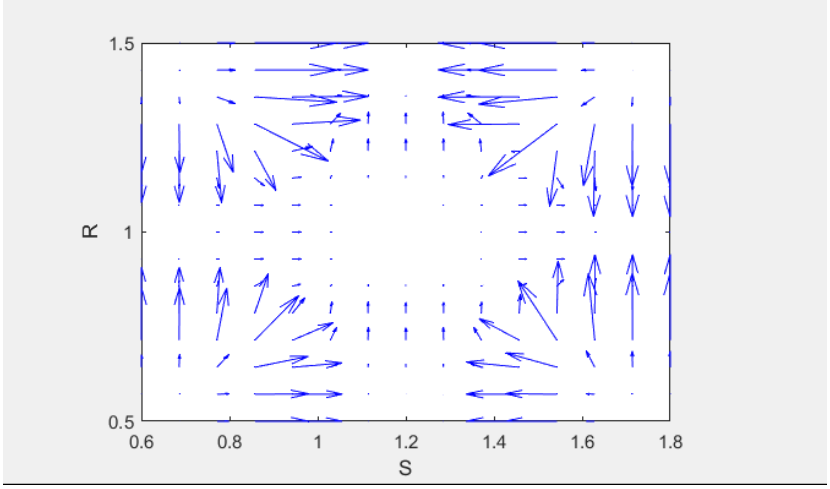

Figure 8. Quiver plot of Nus-1 for S, R.

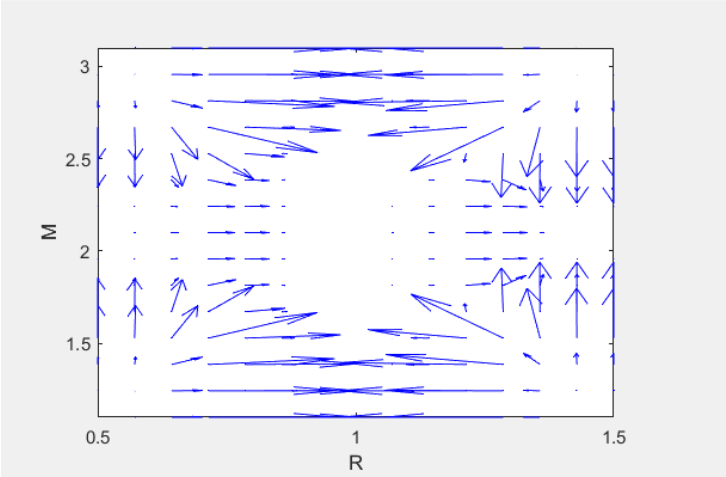

Figure 9. Quiver plot of Nus-1 for R, M.

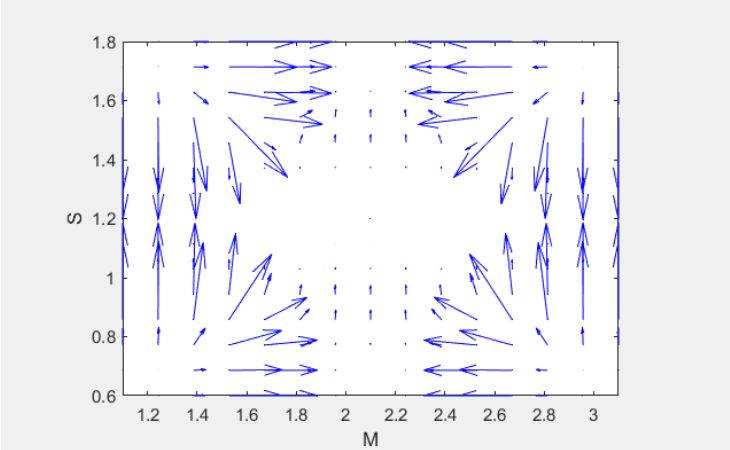

Figure 10. Quiver plot of Nus-1 for M, S.

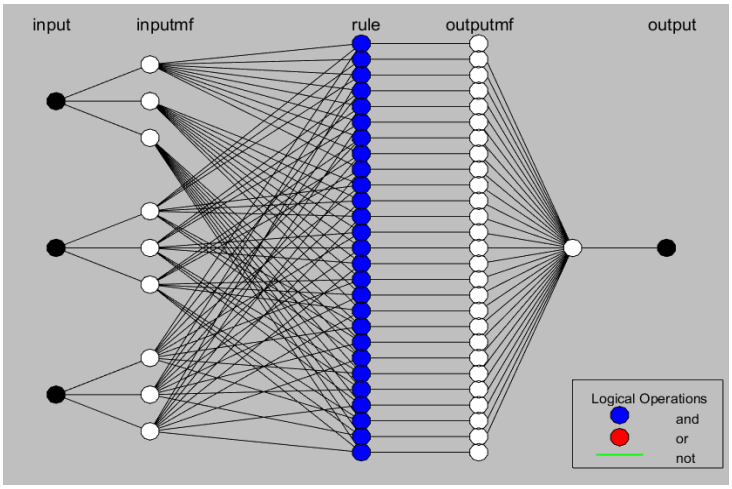

Figure 11. ANFIS-PSO neural network Case-2.

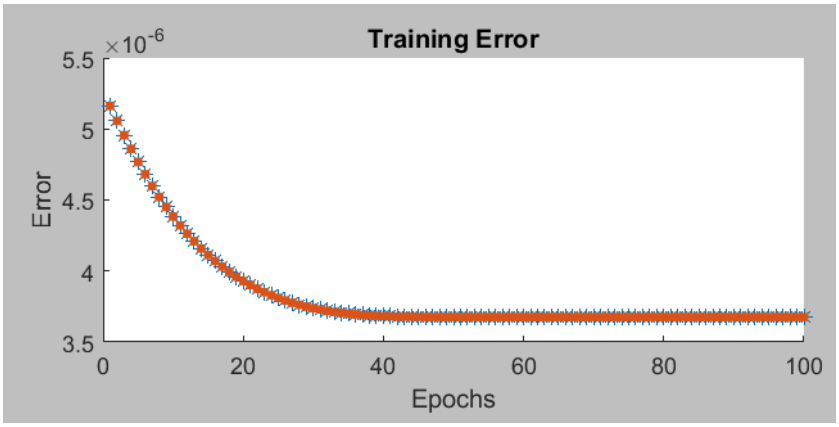

Figure 12. ANFIS-PSO Case-2 error, RMSE=3.675e-06.

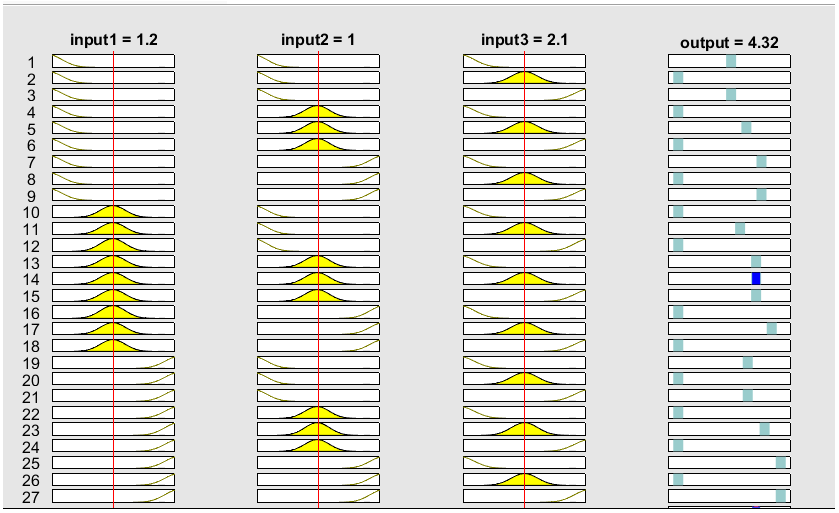

Figure 13. ANFIS-PSO Case-2 rules.

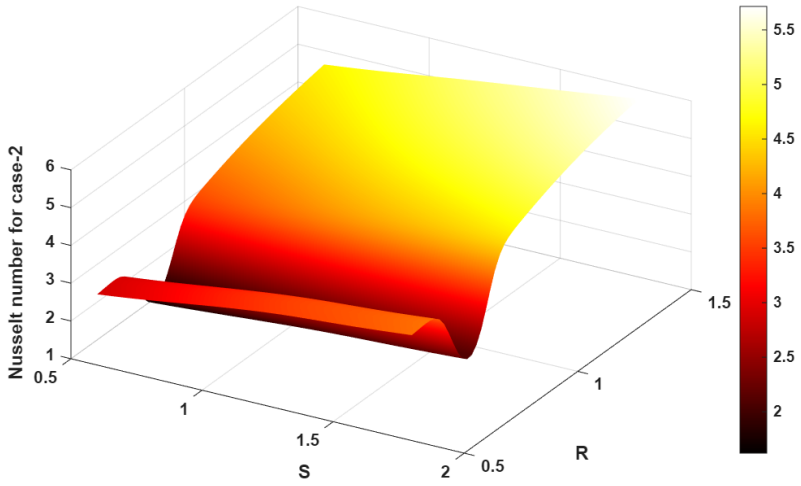

Figure 14. Surface plot of Nus-2 for S, R.

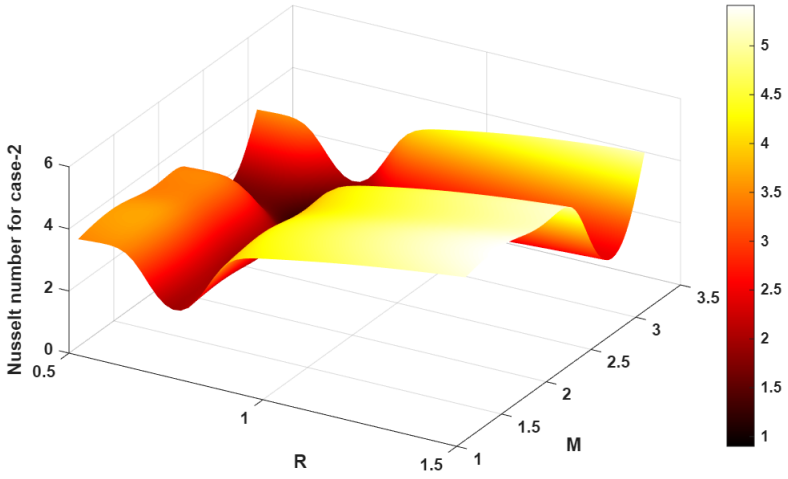

Figure 15. Surface plot of Nus-2 for R, M.

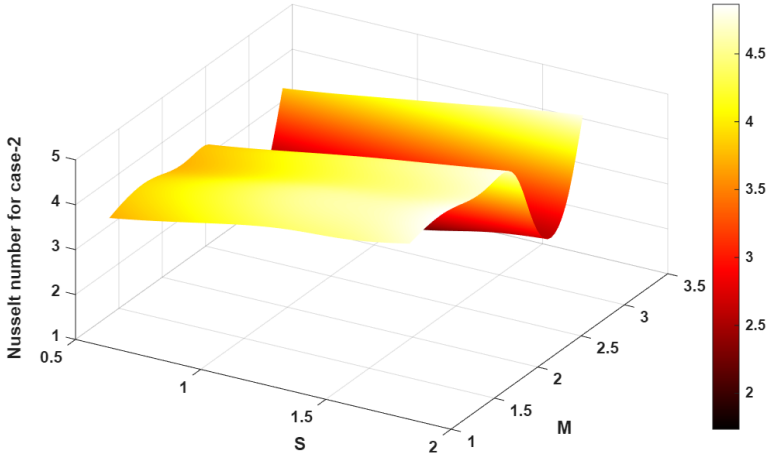

Figure 16. Surface plot of Nus-2 for M, S.

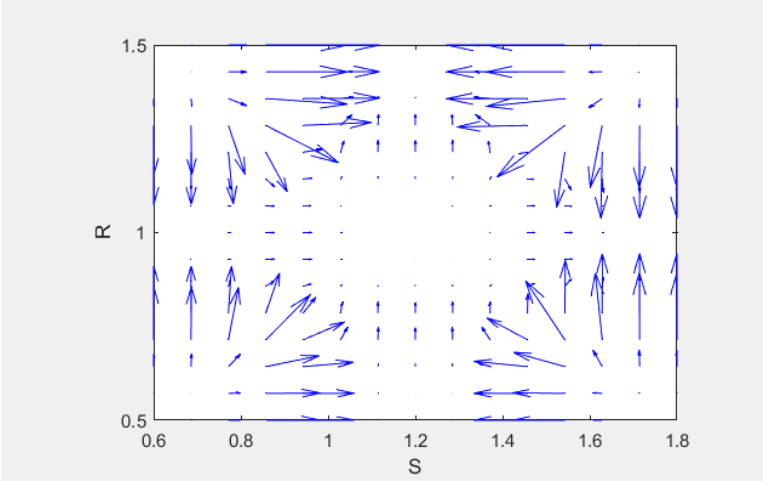

Figure 17. Quiver plot of Nus-2 for S, R.

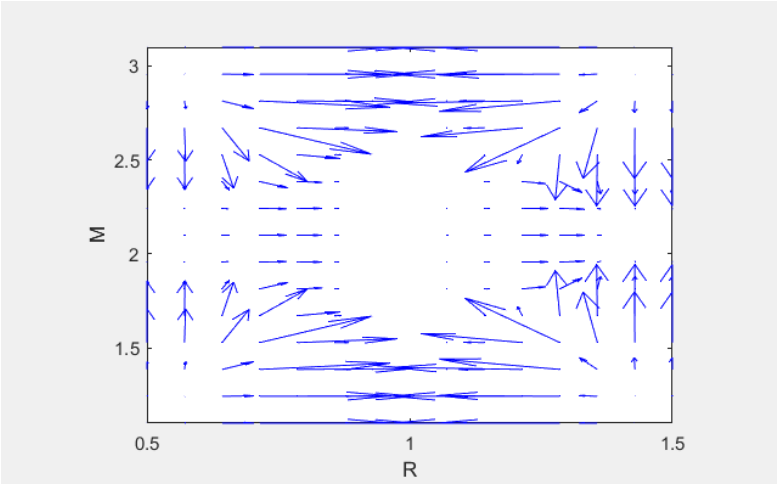

Figure 18. Quiver plot of Nus-2 for R, M.

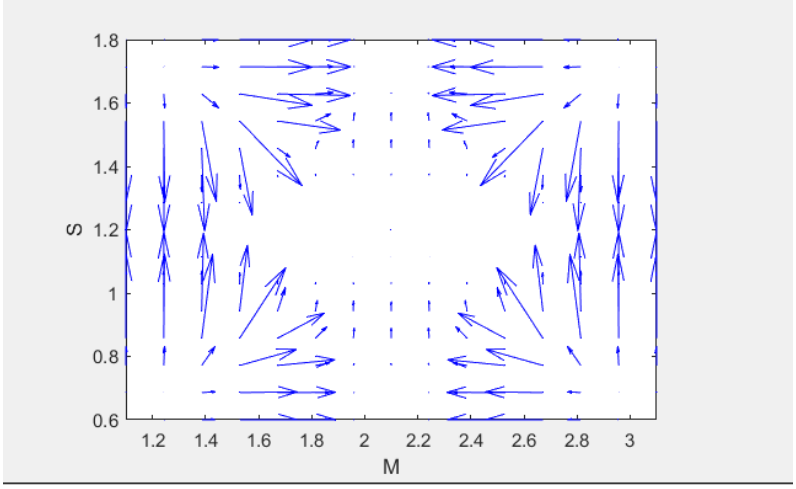

Figure 19. Quiver plot of Nus-2 for M, S.

4.2. The impact of different factors on velocity and temperature profiles

The Nusselt number's fluctuation with parameter A is depicted with (Casson) and without Casson in Case-1 and Case-2, respectively, in Figure 20. Casson fluid exhibits a slightly higher value of heat transfer rates compared to the non-Casson scenario, and *Nus* is observed to decline with the increase in A. In Case-1 (with Casson) and Case-2 (without Casson), Figure 21 displays the Nusselt number with the effect of parameter B. In contrast to the non-Casson scenario, the heat transfer rates in the Casson fluid case show a steady increase, and *Nus* falls as B rises. Figure 22 depicts the correlation between the Nusselt number and the Eckert number (Ec) when using Case-1 (with Casson) and Case-2 (without Casson). Nus values are slightly higher in the Casson fluid, and the experiment's findings show that Nus falls as Ec rises, indicating that heat transfer is reduced by greater viscosity dissipation. The correlation between the Nusselt number and the magnetic parameter (M) is shown in Figure 23 in Case-1 (Casson) and Case-2 (without Casson). Although the *Nus* values in the Casson fluid are somewhat higher, it is discovered that Nus decreases with M, and this indicates that the intensified magnetic effects inhibit the heat transfer. Figure 24 shows the relationship between the Nusselt number

and the radiation parameter (R) in Case-1 (using Casson) and Case-2 (no Casson), respectively. Based on the findings, Nus is increasing with R, showing that there is more thermal radiation to improve heat transfer. Casson fluid is marginally superior. Figure 25 demonstrates how parameter A affects the temperature profile of Case-1 (with Casson) and Case-2 (without Casson). The enhancement of A enhances the temperature fields, and the Casson fluid exhibits slightly better thermal fields as compared to the non-Casson fluid. Figure 26 illustrates how the temperature distribution in Case-1 (with Casson) and Case-2 (without Casson) is impacted by parameter B. In contrast to the non-Casson scenario, the Casson fluid has higher temperature values, and the data indicate that the thermal boundary layer expands as B increases. Figure 27 shows how the Eckert number (Ec) affects the temperature profiles in Casson and non-Casson scenarios. As it is growing in size, the temperature profile increases because there is more dissipation, which is more viscous, converting more kinetic energy to internal energy, and generating more fluid heating. The effect of the parameter (film thickness) on the temperature profile under Casson and non-Casson conditions is shown in Figure 28. The temperature profile rises as Case-2 grows, demonstrating that the bigger the fluid film thickness in the boundary layer, the higher the film's thermal resistance and heat retention. The effect of the magnetic parameter (M) on the velocity gradient in Casson and non-Casson fluids is shown in Figure 29. Because M lowers the velocity profile, the fluid's motion is counteracted by the Lorentz force associated with the magnetic field, which lowers the velocity and flow resistance. Figure 30 shows how the magnetic parameter (M) affects the temperature profile in Casson and non-Casson circumstances. The Lorentz force causes resistive heating, which transforms kinetic energy into thermal energy and raises the nanofluid's overall temperature. The temperature distribution rises in tandem with M. The impact of the radiation parameter (R) on the temperature distribution is depicted in Figure 31. The rise in temperature with increased R indicates that more intense thermal radiation will enhance the energy transfer in fluids and raise the temperature with radiative heat absorption. Figure 32 shows how the unsteadiness parameter (S) affects the Casson and non-Casson nanofluid velocity gradient. The velocity profile lowers as a result of S increasing, indicating that the fluid's motion is restrained by increasing unsteadiness brought on by changes in flow time, which reduces momentum transfer within the boundary layer. The impact of the unsteadiness parameter (S) on the temperature distribution of Casson and non-Casson nanofluids is shown in Figure 33. The temperature profile's increasing S indicates that convective cooling increases with unsteadiness because of a reduced thermal boundary layer and accelerated heat loss. Figure 34 shows how the velocity gradient of Casson and non-Casson nanofluids is affected by the inclined magnetic angle. As ω rises, the velocity profile decreases. This suggests that the Lorentz force is increased by a greater magnetic tilt, suppressing the flow and lowering the flow velocity on the surface.

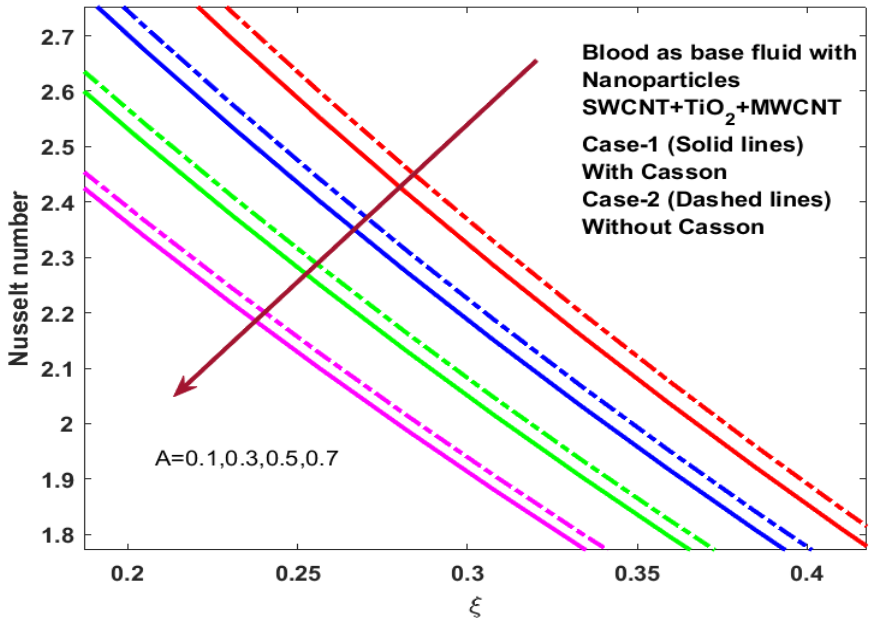

Figure 20. Nus plot for A.

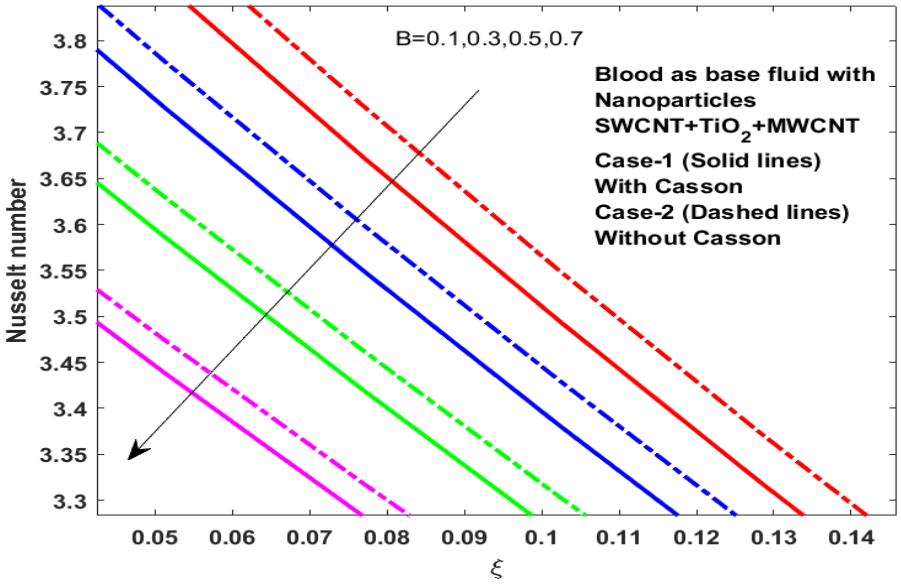

Figure 21. Nus plot for B.

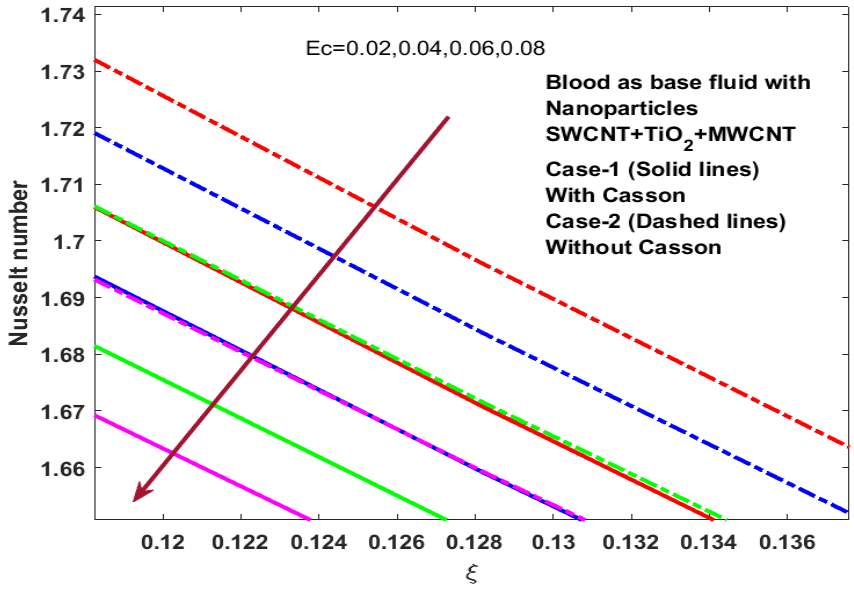

Figure 22. Nus plot for Ec.

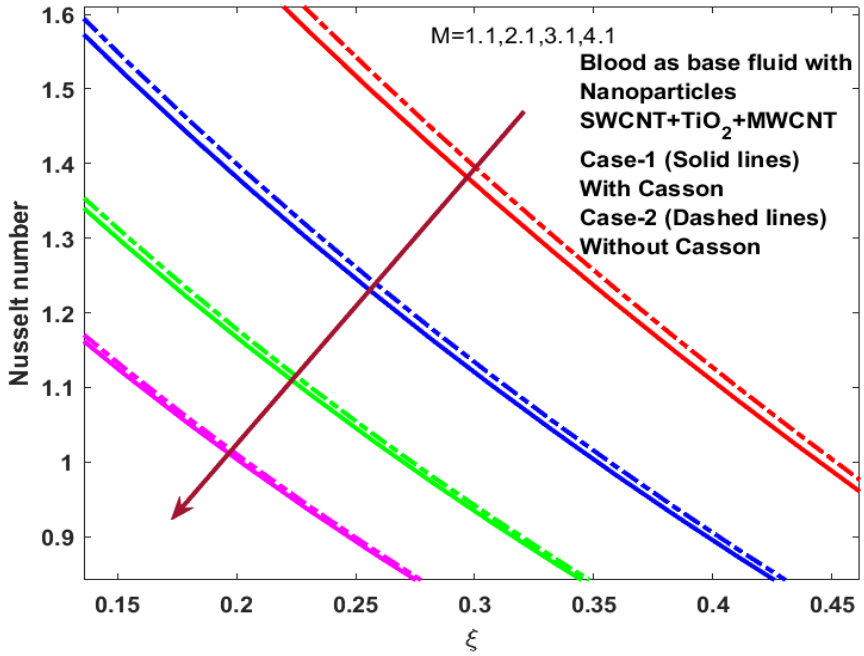

Figure 23. Nus plot for M.

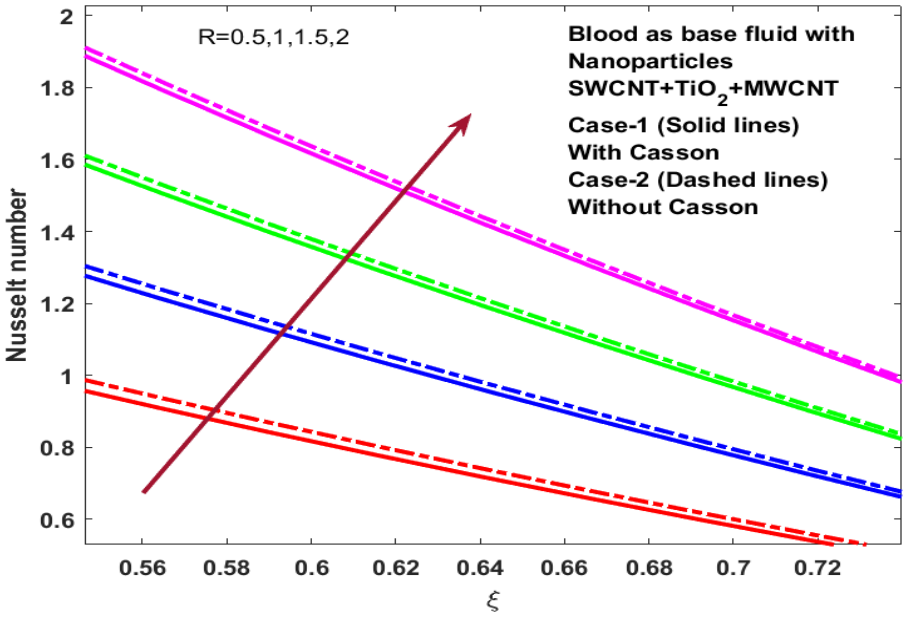

Figure 24. Nus plot for R.

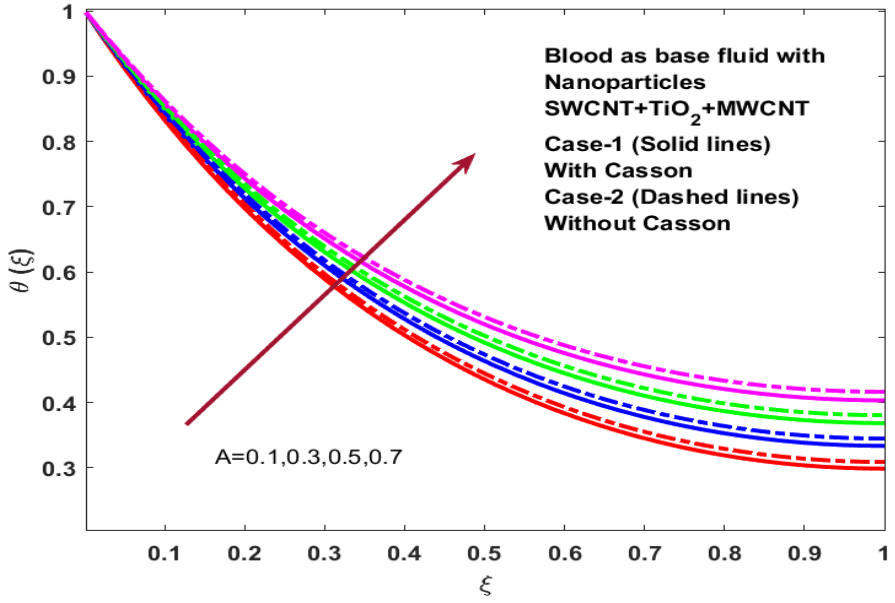

Figure 25. Impact of A on $\theta(\xi)$.

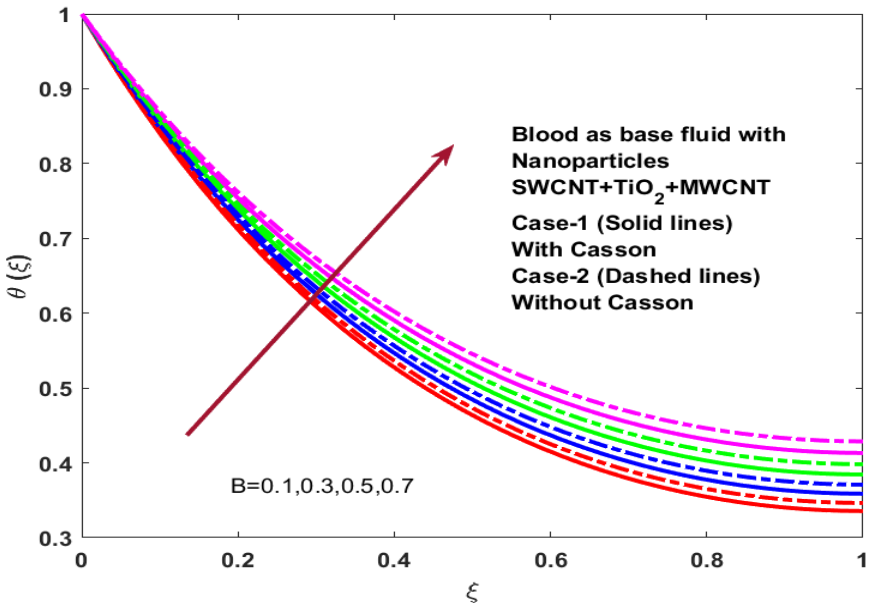

Figure 26. Impact of B on $\theta(\xi)$.

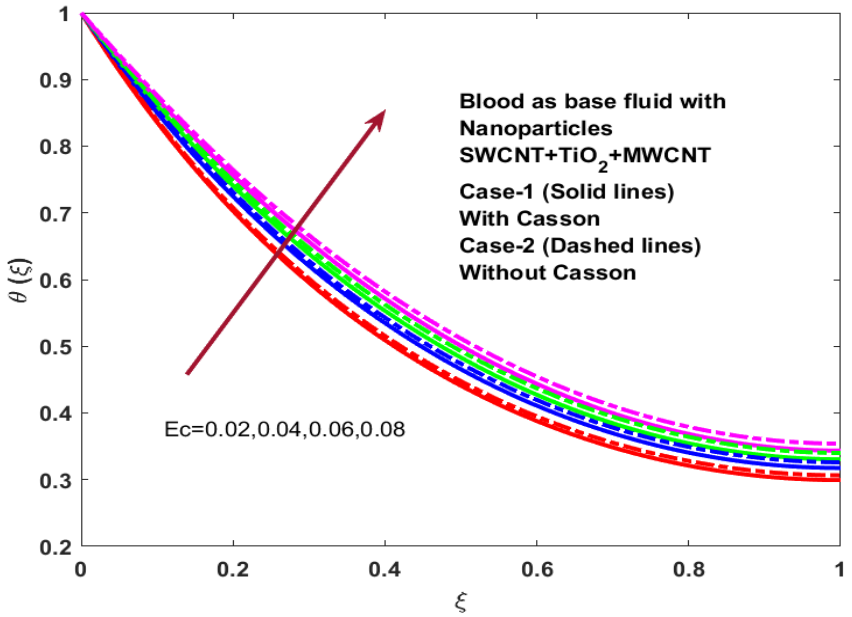

Figure 27. Impact of Ec on $\theta(\xi)$.

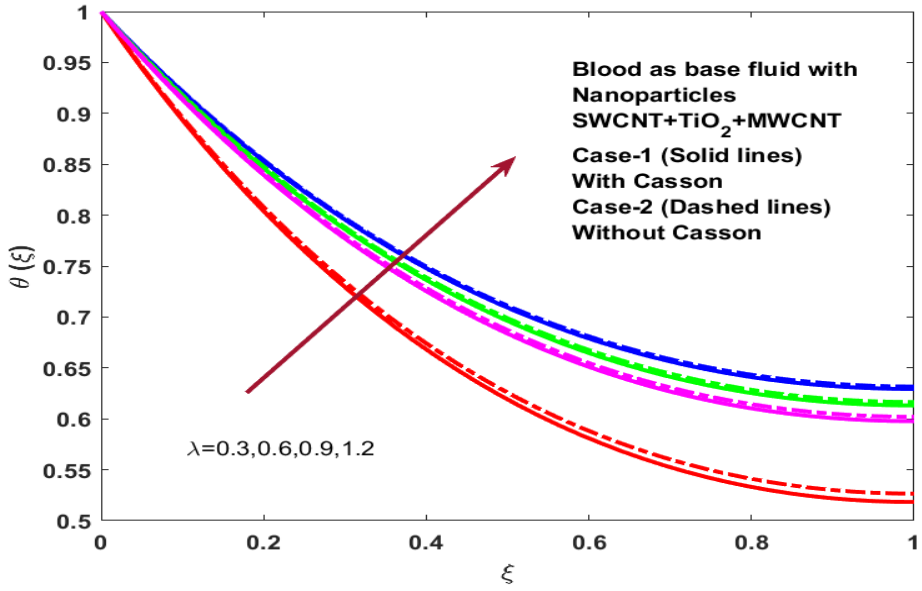

Figure 28. Impact of λ on $\theta(\xi)$.

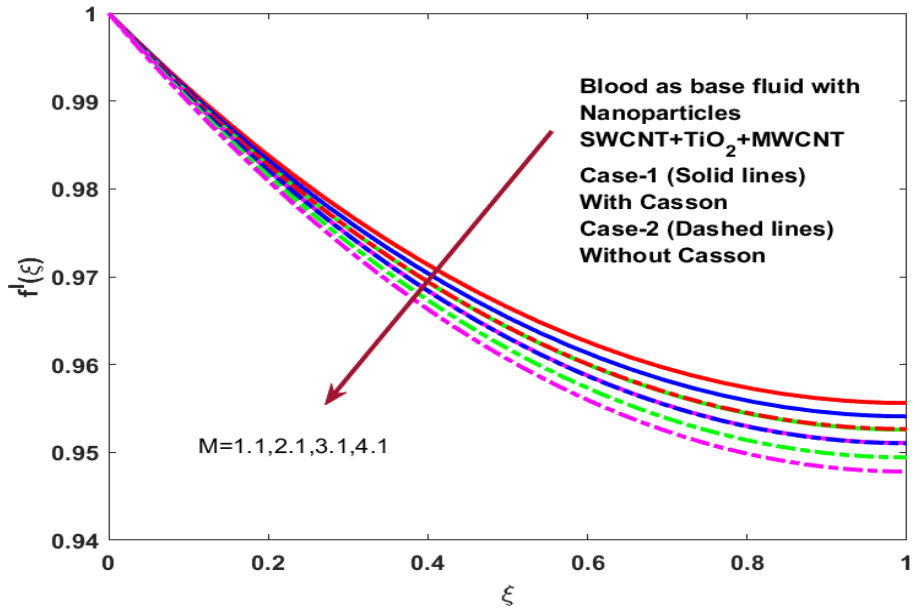

Figure 29. Impact of M on $f'(\xi)$.

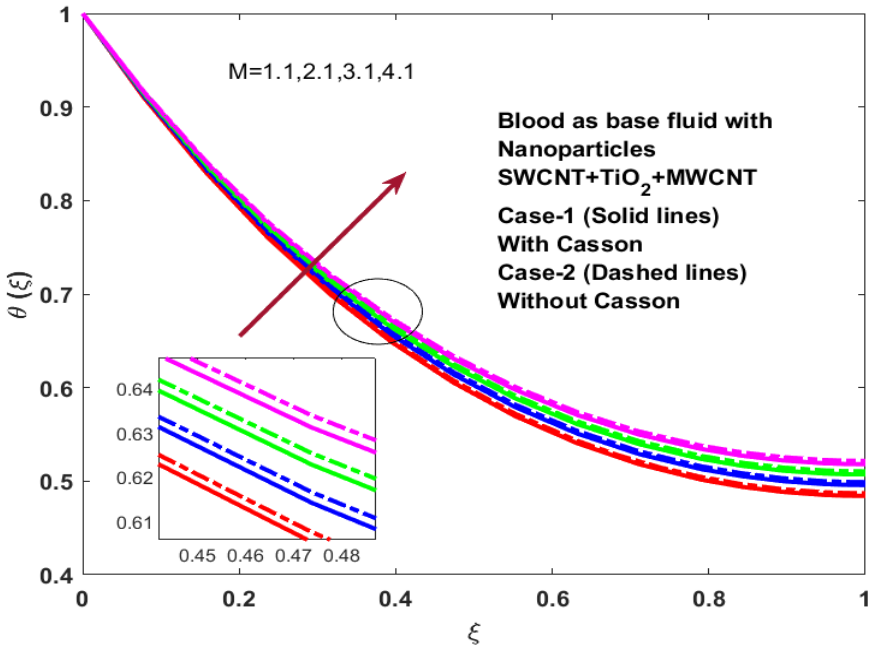

Figure 30. Impact of M on $\theta(\xi)$.

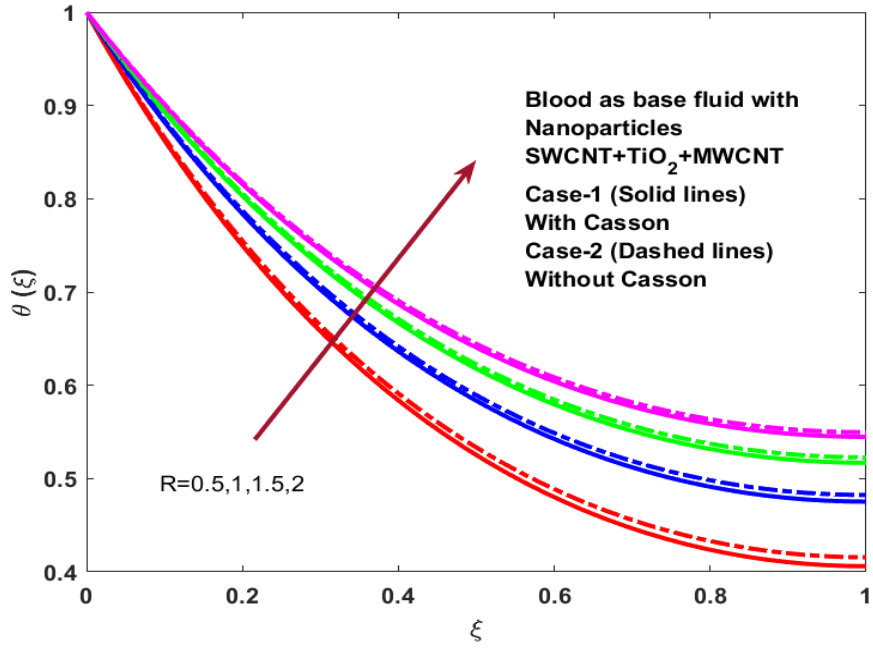

Figure 31. Impact of R on $\theta(\xi)$.

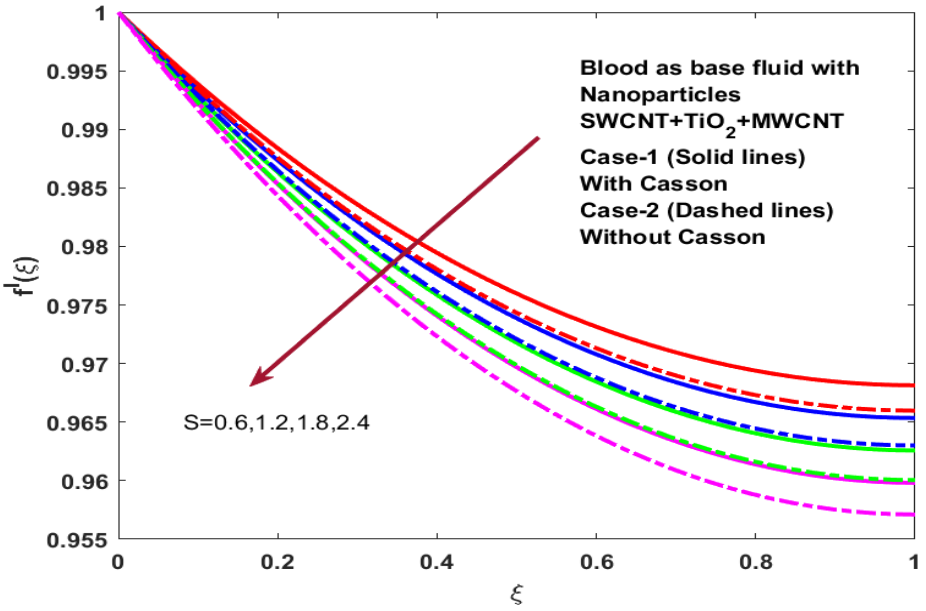

Figure 32. Impact of S on $f'(\xi)$.

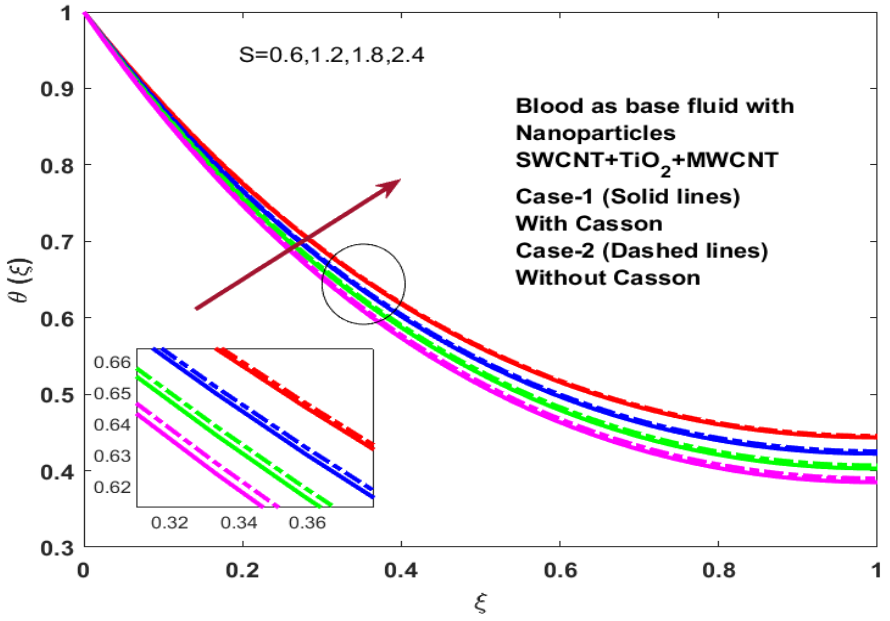

Figure 33. Impact of S on $\theta(\xi)$.

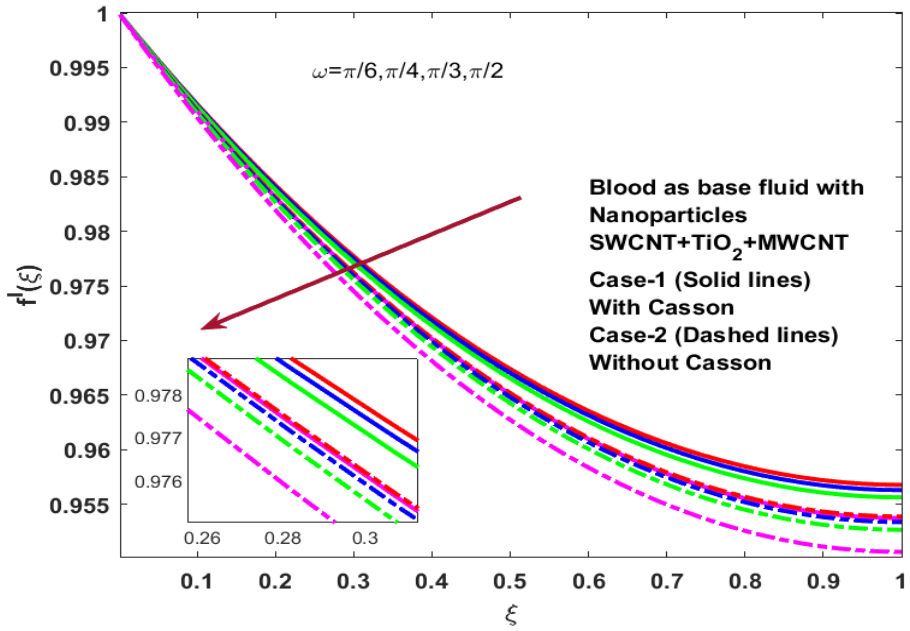

Figure 34. Impact of ω on $f'(\xi)$.

Thermophysical properties of base fluid Blood, $SWCNT$, $MWCNT$, and TiO_2 (titanium dioxide) are listed in Table 1. In Table 2, key factor values (M, S, and R) at various levels are listed. In Table 2, the heat transfer rate, the experimental configuration, and the obtained simulated results are displayed. In most of the runs in Table 3, it is discovered that Case-2's heat transmission rate is 1% more than Case-1. Table 4 validates the present modeled results with the previous study under the specific condition.

Table 1. The thermophysical properties of the basic fluids and the nanoparticles from the investigation of Waqas et al. [32], and Ibrahim and Khan et al. [33].

	Nomenclature of nano-particles and base fluid	$\rho\ (kg/m^3)$	$C_p\ (J/kgK)$	$K\ (W/mK)$	(S/m)
Base fluid	Blood	1063	3594	0.492	0.8
Nanoparticles	SWCNT	2600	425	6600	$5.96*10^7$
	TiO_2	4250	686.2	8.9538	10^{-12}
	MWCNT	1600	796	3000	$1.9*10^{-4}$
Case-1 Ternary hybrid nanofluid with Casson					
Case-2 Ternary hybrid nanofluid without Casson					

Table 2. Key factors.

Key factor	Symbols	Coded values		
		Low	Medium	High
		-1	0	1
S	Z_1	0.6	1.2	1.8
R	Z_2	0.5	1	1.5
M	Z_3	1.1	2.1	3.1

Table 3. Comparing the ANFIS-PSO and numerical results.

S. No	Coded values			Real values			Response (Truth values)		Response (Predicted values)	
	Z1	Z2	Z3	S	R	M	Nus-1	Nus-2	Nus-1	Nus-2
1	−1	−1	−1	0.6	0.5	1.1	2.335276	2.931704	2.335276	2.931703
2	1	−1	−1	1.8	0.5	1.1	3.789065	3.852892	3.78906	3.852896
3	−1	1	−1	0.6	1.5	1.1	4.549166	4.612886	4.549166	4.612886
4	1	1	−1	1.8	1.5	1.1	5.634531	5.680748	5.63453	5.680748
5	−1	−1	1	0.6	0.5	3.1	2.861959	2.931497	2.86195	2.931496
6	1	−1	1	1.8	0.5	3.1	3.788961	3.852772	4.412097	3.939333
7	−1	1	1	0.6	1.5	3.1	4.548790	4.612473	4.548790	4.612471
8	1	1	1	1.8	1.5	3.1	5.634283	5.680473	5.264728	5.629372
9	−1	0	0	0.6	1	2.1	3.710496	3.776615	3.71049	3.776614
10	1	0	0	1.8	1	2.1	4.730956	4.784559	4.748794	4.806606
11	0	−1	0	1.2	0.5	2.1	3.366437	3.431792	3.366437	3.431791
12	0	1	0	1.2	1.5	2.1	5.127604	5.180832	5.12760	5.180832
13	0	0	−1	1.2	1	1.1	4.259666	4.317910	4.259666	4.317909
14	0	0	1	1.2	1	3.1	4.259452	4.317671	4.259452	4.317673
15	0	0	0	1.2	1	2.1	4.259559	4.317791	4.259559	4.317790
16	0	0	0	1.2	1	2.1	4.259559	4.317791	4.259559	4.317790
17	0	0	0	1.2	1	2.1	4.259559	4.317791	4.259559	4.317790
18	0	0	0	1.2	1	2.1	4.259559	4.317791	4.259559	4.317790
19	0	0	0	1.2	1	2.1	4.259559	4.317791	4.259559	4.317790
20	0	0	0	1.2	1	2.1	4.259559	4.317791	4.259559	4.317790

Table 4. Comparison of temperature gradient for $-\theta'(0)$ when $M = R = \varphi = 0$.

S	Kumar et al. [4]	Xu et al. [34]	Present results
1.0	2.6721	2.67722	2.67722
1.2	1.99959	1.99959	1.99959
1.4	1.44774	1.44775	1.44775
1.6	0.95669	0.95669	0.95669
1.8	0.48453	0.48453	0.48453

5. Conclusions

The flow dynamics and heat transmission of a ternary hybrid nanofluid across an unstable thin-film flow are investigated in this work, taking into consideration the absence of Casson effects over a surface, the presence of radiation, a magnetic field, and an uneven heat source or sink. The modified governing equations are solved using MATLAB software's built-in BVP4C solver, and the numerical results are predicted using an adaptive neuro-fuzzy inference system with particle swarm optimization (ANFIS-PSO). Forecast accuracy for intricate heat transfer processes in nanofluid applications is enhanced by the combined ANFIS-PSO model. Because the Casson model depicts blood's non-Newtonian features within microvascular or coating-like layers, it has biomedical importance in thin film flows. Examining the behavior of blood films on various biological surfaces makes research on physiological lubrication and medical coating applications easier.

The outcome of the flow model is summarized as:

1) A greater heat transmission rate was seen in instance 2.
2) Heat source/sink, Eckert number, film thickness, magnetic parameter, and unsteadiness all caused the Nusselt number to drop, whereas the radiation parameter caused it to rise.
3) When the Eckert number, radiation, heat source/sink, film thickness, magnetic parameter, and unsteadiness grew, so did the temperature of the ternary nanofluids.
4) The velocity of ternary nanofluid declined with a rise in magnetic and unsteadiness parameters.
5) ANFIS-PSO forecasted the truth values accurately.

Applications of this study:

1) Targeted drug delivery systems.
2) Hyperthermia-based cancer therapy.
3) Blood-compatible nano coatings for implants.
4) Biomedical sensors and biosensing platforms.
5) Artificial blood substitutes/oxygen carriers.

Future scope of this study:

1) Future work can be done by including the non-linear thermal radiation effect.
2) Deep Neural Networks in machine learning can be applied.
3) Non-linear dynamics analysis of the tetra and pent hybrid nanofluid combination can be done.
4) Cavity analysis can be done through the finite difference and finite element methods.
5) The present work can extend to various non-Newtonian fluids.

Nomenclature

Symbol	Description	SI units
$u_w = \frac{bx}{(1-\alpha t)}$	Velocity along the wall	m/s
$\overline{v}$	velocity along the y-axis	m/s
$\overline{u}$	The velocity in the direction of x	m/s
$\varphi = \varphi_{SWCNT} + \varphi_{TiO_2} + \varphi_{MWCNT}$	The overall volume percentage of nanoparticles	–
B_0	The magnetic field	$T^2\,(Tesla\ Squared)$
T_0	The ambient temperature	$K\,(Kelvin)$
T_w	The temperature of the wall	$K\,(Kelvin)$
q'''	Uneven heat sink or source	Wm^{-3}
$h(t)$	The thickness of the film	m
σ^*	The constant of Stefan-Boltzmann	$Wm^{-2}K^{-4}$
k^*	The mean absorption constant	m^{-1}
ANFIS-PSO	A System for Adaptive Neuro-Fuzzy Inference Based on Particle Swarm Optimization	–
Nu_x, Nus	Nusselt number	–
MHD	Magnetism's hydrodynamic dynamics	–
Nus-1	The Nusselt number for Case-1	–
Nus-2	The Nusselt number for Case-2	–
σ_{THNF}	The electric conductivity of the ternary hybrid nanofluid	S/m
σ_f	The electrical conductivity of the base fluid	S/m
$(\rho C_p)_{THNF}$	The specific heat of the Ternary Hybrid Nanofluid	J/m^3K
$(\rho C_p)_f$	The specific heat of the base fluid	J/m^3K
k_{THNF}	The thermal conductivity of the ternary hybrid nanofluid	W/mK
k_f	The thermal conductivity of the base fluid	W/mK

Continued on next page

Symbol	Description	SI units
ρ_{THNF}	Density of ternary hybrid nanofluid	kg/m^3
ρ_f	The density of the base fluid	kg/m^3
μ_{THNF}	The viscosity of the ternary hybrid nanofluid	$kgm^{-1}s^{-1}$
μ_f	The viscosity of the base fluid	$kgm^{-1}s^{-1}$
Re_x	The Reynolds number	−
λ	The film thickness parameter	−
R	Radiation parameter	−
β_1	Casson's parameter	−
M	The parameter for magnetic	−
Ec	Eckert number	−
Pr	Prandtl's number	−
S	The parameter for unsteadiness	−
ξ	Dimensionless distance parameter	−

Author contributions

Maddina Dinesh Kumar: Writing–original draft, methodology, resources, Software, visualisation, validation; S. Mamatha Upadhya: Writing–original draft, methodology, investigation, formal analysis; Nehad Ali Shah: Investigation, supervision, formal analysis, conceptualization; C. S. K. Raju: Validation, conceptualization, methodology, formal analysis; Se-Jin Yook: Writing–review & editing, software, supervision, project administration. Maddina Dinesh Kumar and Nehad Ali Shah contributed equally to this work and are co-first authors. All authors have read and approved the final version of the manuscript for publication.

Use of Generative-AI tools declaration

The authors declare they have not used Artificial Intelligence (AI) tools in the creation of this article.

Acknowledgments

This research was supported by the "Regional Innovation System & Education (RISE)" through the Seoul RISE Center, funded by the Ministry of Education (MOE) and the Seoul Metropolitan Government (2025-RISE-01-027-04).

Conflict of interest

The authors declare no conflicts of interest.

References

1. C. Y. Wang, Liquid film on an unsteady stretching surface, *Quart. Appl. Math.*, **48** (1990), 601–610. https://doi.org/10.1090/qam/1079908
2. H. I. Andersson, J. B. Aarseth, B. S. Dandapat, Heat transfer in a liquid film on an unsteady stretching surface, *Int. J. Heat Mass Tran.*, **43** (2000), 69–74. https://doi.org/10.1016/S0017-9310(99)00123-4
3. M. S. Abel, J. Tawade, M. M. Nandeppanavar, Effect of non-uniform heat source on MHD heat transfer in a liquid film over an unsteady stretching sheet, *Int. J. Nonlin. Mech.*, **44** (2009), 990–998. https://doi.org/10.1016/j.ijnonlinmec.2009.07.004
4. K. A. Kumar, N. Sandeep, V. Sugunamma, I. L. Animasaun, Effect of irregular heat source/sink on the radiative thin film flow of MHD hybrid ferrofluid, *J. Therm. Anal. Calorim.*, **139** (2020), 2145–2153. https://doi.org/10.1007/s10973-019-08628-4
5. M. K. Prasad, S. H. Naveenkumar, C. S. K. Raju, S. M. Upadhya, Nonlinear thermal convection on unsteady thin film flow with variable properties, *J. Phys.: Conf. Ser.*, **1427** (2020), 012016. 0
6. G. Gomathy, B. R. Kumar, Impacts of nanoparticle shapes on Ag-water nanofluid thin film flow through a porous medium with thermal radiation and ohmic heating, *J. Therm. Anal. Calorim.*, **149** (2024), 6877–6895. https://doi.org/10.1007/s10973-023-12609-z
7. A. Bhandari, Effect of thin film thickness of ferrofluid on inclined bioconvective flow, *Chinese J. Phys.*, **92** (2024), 959–974. https://doi.org/10.1016/j.cjph.2024.10.019
8. F. Z. Wang, A. M. Saeed, V. Puneeth, N. A. Shah, M. S. Anwar, K. Geudri, et al., Heat and mass transfer of Ag-H_2O nano-thin film flowing over a porous medium: A modified Buongiorno's model, *Chinese J. Phys.*, **84** (2023), 330–342. https://doi.org/10.1016/j.cjph.2023.01.001
9. M. Qayyum, A. Tahir, A. Bariq, A. Akgül, S. T. Saeed, Modelling and analysis of thin film flow of Fuzzified Johnson Segelman nanofluid using a fuzzy extension of the He-Laplace scheme, *Math. Comp. Model. Dyn.*, **29** (2023), 286–314. https://doi.org/10.1080/13873954.2023.2276440
10. D. Pal, D. Chatterjee, Magneto-thermos heat transfer of a chemically reactive and viscous dissipative Casson nanofluid thin film over an unsteady stretching surface with variable thermal conductivity, *J. Nanofluids*, **12** (2023), 1973–1986. https://doi.org/10.1166/jon.2023.2055
11. P. Bathmanaban, E. P. Siva, S. S. Santra, S. S. Askar, A. Foul, S. Nandi, Heat and mass transfer in double-diffusive mixed convection of Casson fluid: biomedical applications, *Colloid Polym. Sci.*, **302** (2024), 1635–1669. https://doi.org/10.1007/s00396-024-05286-3
12. R. K. Dash, K. N. Mehta, G. Jayaraman, Casson fluid flow in a pipe filled with a homogeneous porous medium, *Int. J. Eng. Sci.*, **34** (1996), 1145–1156. https://doi.org/10.1016/0020-7225(96)00012-2
13. S. M. Alghamdi, A. Hanif, R. S. Almufarij, E. A. Shokralla, M. D. Alshahrani, I. Ragab, et al., Tuning the microstructure and thermoelectric response of β-$FeSi_2$ thin films via cobalt doping, *J. Mater. Sci.: Mater. Electron.*, **36** (2025), 1807. https://doi.org/10.1007/s10854-025-15897-3

14. F. Z. Duraihem, R. L. V. R. Devi, P. Prakash, T. K. Sreelakshmi, S. Saleem, P. Durgaprasad, et al., Enhanced heat and mass transfer characteristics of multiple slips on hydro-magnetic dissipative Casson fluid over a curved stretching surface, *Int. J. Mod. Phys. B*, **37** (2023), 2350229. https://doi.org/10.1142/S0217979223502296
15. M. A. Fahmy, A computerised DRBEM model for generalised magneto-thermo-visco-elastic stress waves in functionally graded anisotropic thin film/substrate structures, *Lat. Am. J. Solids Stru.*, **11** (2014), 386–409.
16. D. Thenmozhi, M. E. Rao, C. Nagalakshmi, R. R. Devi, P. D. Selvi, Lie similarity analysis of MHD Casson fluid flow with heat source and variable viscosity over a porous stretching sheet, *International Journal of Thermofluids*, **23** (2024), 100804. https://doi.org/10.1016/j.ijft.2024.100804
17. S. U. S. Choi, J. A. Eastman, Enhancing thermal conductivity of fluids with nanoparticles, *ASME International Mechanical Engineering Congress & Exposition*, San Francisco, California, USA, 1995, 99–105. https://doi.org/10.1115/IMECE1995-0926
18. J. Hakami, A. Ashfaq, A. R. Abd-Elwahed, M. D. Alshahrani, E. A. Shokralla, I. Ragab, et al., High-performance Bi-doped SnS thin films: A route to enhanced thermoelectric power for miniaturised devices, *Int. Commun. Heat Mass*, **169** (2025), 109759. https://doi.org/10.1016/j.icheatmasstransfer.2025.109759
19. S. M. Upadhya, S. Suresh, M. D. Kumar, P. D. Selvi, S. S. K. Raju, C. S. K. Raju, et al., Comparison of SWCNT plus MWCNT and SWCNT+MWCNT+Fe_3O_4 nanofluid across a spinning disk with suspended joule heating and non-linear thermal radiation: Multi-linear optimisation, *Numerical Heat Transfer Part B-Fundamentals*, **86** (2025), 1111–1137. https://doi.org/10.1080/10407790.2024.2302858
20. S. G. Krishna, M. Shanmugapriya, R. Sundareswaran, P. S. Kumar, MANFIS approach for predicting heat and mass transport of bio-magnetic ternary hybrid nanofluid using Cu/Al_2O_3/MWCNT nanoadditives, *Biomass Conv. Bioref.*, **14** (2024), 11175–11190. https://doi.org/10.1007/s13399-022-02989-x
21. A. Kumar, M. A. Hassan, Heat transfer in flat tube car radiator with CuO-MgO-TiO_2 ternary hybrid nanofluid, *Powder Technol.*, **434** (2024), 119275. https://doi.org/10.1016/j.powtec.2023.119275
22. A. Mishra, G. Pathak, A comparative analysis of MoS_2-SiO_2/H_2O hybrid nanofluid and MoS_2-SiO_2-GO/H_2O ternary hybrid nanofluid over an inclined cylinder with heat generation/absorption, *Numer. Heat Tr. A-Appl.*, **85** (2024), 2724–2753. https://doi.org/10.1080/10407782.2023.2228483
23. C. M. Mohana, B. R. Kumar, Numerical and semi-analytical approaches for heat transfer analysis of ternary hybrid nanofluid flow: A comparative study, *Math. Comput. Simulat.*, **226** (2024), 66–90. https://doi.org/10.1016/j.matcom.2024.06.019
24. D. Mohanty, G. Mahanta, S. Shaw, Irreversibility and thermal performance of nonlinear radiative cross-ternary hybrid nanofluid flow about a stretching cylinder with industrial applications, *Powder Technol.*, **433** (2024), 119255. https://doi.org/10.1016/j.powtec.2023.119255
25. P. Rana, S. Gupta, G. Gupta, Optimization of heat transfer by nonlinear thermal convection flow past a solid sphere with Stefan blowing and thermal slip using Taguchi method, *Int. Commun. Heat Mass*, **141** (2023), 106580. https://doi.org/10.1016/j.icheatmasstransfer.2022.106580

26. P. Rana, X. Y. Zhu, I. Pop, Multiplicity and stability of solutions in transport phenomena of non-Newtonian Carreau nanofluid with nonlinear Rosseland thermal approximations and neural prediction, *Case Stud. Therm. Eng.*, **68** (2025), 105821. https://doi.org/10.1016/j.csite.2025.105821
27. G. K. Ramesh, R. Saadeh, J. K. Madhukesh, A. Qazza, U. Khan, A. Zaib, et al., Neural network algorithms of a curved Riga sensor in a ternary hybrid nanofluid with chemical reaction and Arrhenius kinetics, *J. Radiat. Res. Appl. Sc.*, **17** (2024), 101078. https://doi.org/10.1016/j.jrras.2024.101078
28. P. Rana, J. P. Ma, Y. R. Zhang, J. Q. Chen, G. Gupta, Finite element and neural computations for energy system containing conductive solid body and bottom circular heaters utilizing Ag-MgO (50:50)/water hybrid nanofluid, *J. Magn. Magn. Mater.*, **577** (2023), 170775. https://doi.org/10.1016/j.jmmm.2023.170775
29. T. Gul, M. Bilal, M. Shuaib, S. Mukhtar, P. Thounthong, Thin film flow of the water-based carbon nanotubes hybrid nanofluid under the magnetic effects, *Heat Transf.*, **49** (2020), 3211–3227. https://doi.org/10.1002/htj.21770
30. R. Ali, A. Shahzad, K. us Saher, Z. Elahi, T. Abbas, The thin film flow of Al_2O_3 nanofluid particle over an unsteady stretching surface, *Case Stud. Therm. Eng.*, **29** (2022), 101695. https://doi.org/10.1016/j.csite.2021.101695
31. A. Divya, T. Jithendra, M. Z. Khan, A. Noorwali, K. M. Othman, A novel prediction model for the analysis of Ree-Eyring fluid with hall current in Darcy-Forchheimer porous media based on machine learning technique, *Propuls. Power Res.*, **14** (2025), 527–551. https://doi.org/10.1016/j.jppr.2025.09.003
32. H. Waqas, S. A. Khan, T. Muhammad, Thermal analysis of magnetized flow of AA7072-AA7075/blood-based hybrid nanofluids in a rotating channel, *Alex. Eng. J.*, **61** (2022), 3059–3068. https://doi.org/10.1016/j.aej.2021.08.033
33. M. Ibrahim, M. I. Khan, Mathematical modelling and analysis of SWCNT-Water and MWCNT-Water flow over a stretchable sheet, *Comput. Meth. Prog. Bio.*, **187** (2020), 105222. https://doi.org/10.1016/j.cmpb.2019.105222
34. H. Xu, I. Pop, X. C. You, Flow and heat transfer in a nano-liquid film over an unsteady stretching surface, *Int. J. Heat Mass Tran.*, **60** (2013), 646–652. https://doi.org/10.1016/j.ijheatmasstransfer.2013.01.046

AIMS Press